Materials Advances

Accepted Manuscript

This article can be cited before page numbers have been issued, to do this please use: A. Nowacka and F. X. Llabrés i Xamena, *Mater. Adv.*, 2026, DOI: 10.1039/D6MA00417B.

ROYAL SOCIETY OF CHEMISTRY

rsc.li/materials-advances

View Article Online
DOI: 10.1039/D6MA00417B

ARTICLE

Hierarchically structured mixed-linker HKUST-1 Metal Organic Frameworks as catalysts: One-pot synthesis of quinazolines

Anna Nowacka [a] and Francesc X. Llabrés i Xamena [*a]

Received 00th January 20xx,
Accepted 00th January 20xx

DOI: 10.1039/x0xx00000x

Hierarchically structured HKUST-1 compounds have been prepared by a mixed-linker strategy starting from mixtures of trimesic (BTC) and 5-hydroxyisophtalic (OH-IP) acids in different proportions. Unlike purely microporous pristine HKUST-1, the mixed-linker compounds feature a micro-/mesoporous system in which mesopores account for up to 40% of the total pore volume of the solid. The creation of mesopores is reflected by the appearance of deep trenches running in well-defined directions, parallel to the edges of the octahedral crystal. This evidences that point defects introduced by the incorporation of OH-IP are not distributed randomly through the framework, but they tend to coalesce into line defects along the <1 1 0> direction. The creation of such a hierarchical system of mesopores translates into a higher catalytic activity of mixed-linker MOFs with respect to pristine HKUST-1 for the conversion of bulky substrates, as we showed for the synthesis of quinazoline by oxidative coupling of benzylamine and 2-aminoacetophenone with tert-butyl hydroperoxide.

1. Introduction

For over two decades, Metal-Organic Frameworks (MOFs) have been recognized for their significant utility as heterogeneous catalysts.[1–3] Their remarkable properties, including exceptionally large surface areas, a high degree of tunability in their pore structure and chemical composition, and the inherent capacity for post-synthesis modification, collectively position MOFs as highly promising candidates for the development of advanced heterogeneous catalysts. These attributes enable the design of catalysts exhibiting superior activity and specificity, thereby addressing the demands of a broad spectrum of applications. However, a substantial quantity of MOFs exhibit microporosity (pore diameter < 2 nm), which can significantly restrict their utility in applications involving bulky substrates.[4] This limitation arises from diffusion constraints and restricted access to the active metal sites within the MOFs.[5] Therefore, considerable efforts have been directed towards expanding the pore dimensions of MOFs into the mesoporous range.[6,7]

One way of achieving this goal involves the controlled generation of large-scale defects within the crystalline framework in a controlled way, leading to the formation of hierarchically structured MOFs. A number of *de novo* methodologies have been reported to date, including ligand extension or hydrolytic post-synthesis methods, among others.[8] One specific technique that has attracted considerable attention is metal-ligand-fragment co-assembly,[9] also known as defective linker approach.[10–13] The method comprises combining the native organic linker of the parent MOFs with a small amount of a truncated defective-inducing linker, which is geometrically equivalent but lacks one or more connecting functional groups. The large-scale arrangement of such defects (e.g., point-defects clustering) can lead to the formation of mesopores within the crystal structure. The resulting defective materials are called hierarchically structured MOFs, in which micro- and mesopores coexist without compromising the crystalline integrity of the material. The presence of mesopores can greatly influence mass transport pathways within the pore system, as well and the framework's rigidity and density, its electronic and magnetic properties, and ultimately the material's catalytic performance.[14–16]

In relevant prior reports, Fang et al.[17] reported on the synthesis of a series of defect-engineered MOFs based on HKUST-1 by mixing the native trimesate struts with various defect-inducing linkers (viz., 5-hydroxyisophtalate and pyridine-3,5-dicarboxylate linkers) in varying ratios, as a way to control simultaneously the properties of the metal nodes and to introduce functionalized mesopores. Analogously, Liu et al.[18] partially replaced trimesate linkers in HKUST-1 by benzoic acid as defective-inducing linker, resulting in hierarchical micro-mesoporous systems with improved external surface area compared to the pristine MOF. Besides HKUST-1, we also reported the use of a mixed-linker synthesis approach to modulate the textural and catalytic properties of zirconium trimesate MOF-808 as heterogeneous catalysts for the Meerwein-Ponndorf-Verley reduction of bulky carbonyl compounds, such as ketosteroids.[4,19]

Herein, we describe the use of a defective-linker approach to prepare copper trimesate HKUST-1 compounds exhibiting hierarchical micro-mesoporosity. We analyze the impact of the induced defects and hierarchical pore structure on the catalytic performance of the modified compounds in a reaction involving sterically hindered products, in comparison to unmodified

[a] Instituto de Tecnología Química (ITQ), Consejo Superior de Investigaciones Científicas-Universitat Politècnica de València, 46022, Valencia, Spain. E-mail: fllabres@itq.upv.es; anna.nowacka21@gmail.com

HKUST-1. For this investigation, we have considered the one-pot oxidative synthesis of quinazoline (with approximate dimensions of 12 x 8 x 3 Å^3) as a model reaction (see Scheme 1), given its molecular dimensions are comparable to the pore openings of HKUST-1 (approximately 9 Å in diameter).

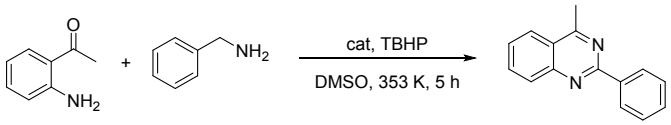

Scheme 1. Typical reaction conditions for the cyclization of 2-aminoacetophenone and benzylamine.

N-heterocycles are present in many natural products and are well known biological active molecules, and quinazolines and quinazolinone skeletons are recurrently found in pharmaceutical literature.[20] Quinazolines are conventional prepared via Bischler cyclization of dicarbonyl compounds and diamines, but novel synthetic pathways are actively being investigated.[21] Thus, Wang et al.[22] reported on a simple and efficient, ligand-free Cu^+ catalyzed Ullman coupling and aerobic oxidation route to quinazoline derivatives, by reacting substituted (2-bromophenyl)methylamines with amides. In another report by Han et al.,[23] CuCl/DABCO/4-HO-TEMPO was used as catalyst for the aerobic oxidative synthesis of 2-substituted quinazolines through a one-pot reaction between aldehydes and 2-aminobenzylamines. Despite the good results obtained with homogeneous catalysts, developing heterogeneous catalysts for the synthesis of quinazoline remains a consistently practical and compelling alternative. In this sense, γ-Fe_2O_3 nanoparticles[24] and polymer-supported bimetallic Pt/Ir alloyed nanoclusters[25] have been reported for this reaction. Also, MOFs have been considered for this reaction. Truong et al. [26] reported on the use of cobalt-containing ZIF-67 for the cyclization of 2-aminobenzoketones and benzylamines, yielding 2-arylquinazolines, with results indicating high activity and reusability.

2. Experimental

2.1. Synthesis

We have used the mixed-linker solid solution method to prepare two hierarchically structured copper-containing HKUST-1 compounds, referred to as **HM-1** and **HM-2**. A pristine, linker pure HKUST-1 material, named **M-1**, was also prepared for comparison. We followed a slightly modified method reported earlier,[17] using mixtures of trimesic acid (H_3BTC) and 5-hydroxyisophthalic acid (OH-IP) in different proportions. For the synthesis of the pristine **M-1** compound, $Cu(NO_3)_2{\cdot}2.5\ H_2O$ (5 mmol) was dissolved in 25 mL H_2O. Then, a second solution of H_3BTC (2.5 mmol) in 25mL of DMF was prepared, and both solutions were mixed under stirring, transferred into an autoclave and placed inside an oven at 373 K for 4 h. The blue precipitate obtained was filtered off, thoroughly washed with DMF and soaked three times for 6 hours with methanol and dried under a vacuum at 573 K overnight before use.

Mixed-linker **HM-1** and **HM-2** compounds were prepared and purified using an analogous procedure and starting from a mixture of linkers with different BTC:OH-IP ratios of 70:30 and 50:50, respectively.

2.2. Characterization

Powder X-ray diffraction (PXRD) was used to confirm the expected structure and crystallinity of the materials. Powder materials analysis were performed on PANalytical Cubix fast diffractometer, using CuKα1 radiation (λ= 1,5406Å) and an X'Celerator detector with Bragg-Brentano geometry. XRD patterns recorded in the 2θ range from 2 to 60 were analyzed using X'pert Highscore Plus software. The corresponding thermogravimetric curves (TGA) of the MOFs were measured in the temperature range 300-700 K under an air flow and a heating ramp of 10 K min^{-1} using a Netzsch STA 449 F3 Jupiter analyzer. The BTC:OH-IP ratios of samples **HM-1** and **HM-2** were determined by Nuclear Magnetic Resonance (NMR) on a Bruker Avance spectrometer of 300 MHz frequency using TMS as internal standards and normalizing the signals to the DMSO-d6 signal. To do this, liquid phase ^{1}H NMR spectra were measured for the samples (30 mg) digested in d_2-H_2SO_4 (0.1 mL) and d_6-DMSO (0.5 mL) mixtures. N_2 adsorption-desorption isotherms at 77 K were collected on a Micrometrics Gemini V gas adsorption analyzer. The specific surface area (S_{BET}) was obtained using the BET method (in the P/P_0 0.01 to 0.1 range) after fulfilling the four consistency criteria recommended by Rouquerol.[27,28] Pore size distribution was determined from the BJH method applied to the adsorption branch.[29] Specific external surface area (S_{ext}) and micropore volume (V_{micro}) were determined from the corresponding t-plot analysis. Morphology of the samples was analyzed by Field Emission Scanning Electron Microscopy (FESEM) using a Zess Ultra55 instrument. In the leaching experiment, metal traces in the reaction filtrate were analyzed by ICP-OES on a Varian 715-ES instrument.

2.3 Catalytic reaction

In a typical catalytic test, 20 mg of the as prepared catalyst was added to a glass reactor containing a mixture of 2-aminoacetophenone (122 µL, 1 mmol), benzylamine (164 µL, 1.5 mmol), tert-butyl hydroperoxide (TBHP) 70% in water (685 µL, 5 mmol), and diphenyl ether (100 µL) as internal standard in DMSO (2 mL). The reaction mixture was stirred for 5 h at 400 rpm (enough to avoid external diffusion control of the reaction), at 353 K. The reaction conversion was monitored by withdrawing aliquots from the reaction mixture at different time intervals, quenched with an aqueous KOH solution (5%, 1 mL), dryed over anhydrous Na_2SO_4, and analyzed by GC with reference to diphenyl ether. An Agilent 7890A instrument equipped with a Flame Ionization Detector (FID) and a HP5 column (30 m x 0.25 mm x 0.25 µm) was used.

3. Results and discussion

3.1. Synthesis and characterization

Pristine HKUST-1 (**M-1**) and mixed-linker **HM-1** and **HM-2** samples were obtained as described in the Experimental

View Article Online
DOI: 10.1039/D6MA00417B

Section. The corresponding PXRD patterns shown in Fig. 1 are in perfect agreement with the pattern simulated for HKUST-1, indicating that all materials are isoreticular, pure compounds with high crystallinity. The XRD patterns show no evidences of peak splitting or any significant peak broadening, thus ruling out the formation of a mixture of two phases. Moreover, an eventual phase pure OH-IP copper MOF would necessarily have a different crystalline structure, leading to the appearance of additional peak lines not attributable to the HKUST-1 material, which are not observed in any case.

The amounts of OH-IP incorporated in **HM-1** and **HM-2** were determined from the peak intensity ratio in the corresponding ^{1}H NMR spectra after digestion of the samples in d_2-H_2SO_4/d_6-DMSO mixtures (Fig. S1 in the Supplementary Material). The analysis revealed that **HM-1** and **HM-2** contained 10% and 15% of the OH-IP linker, respectively.

The thermal stability of the pristine and mixed-linker samples was determined from the TGA curves (Fig. S2). All three samples showed the typical two-steps weight loss expected for HKUST-1 compounds: a first weight loss of *ca*. 30wt% at around 350 K, due to coordinated water; and a second weight loss of *ca*. 45wt% between 550-600 K due to linker decomposition. The compared TGA curves indicate that the thermal stability of mixed-linker samples with respect o pristine HKUST-1 gradually decreases with the amount of OH-IP incorporated in the structure, as it can be better appreciated in the derivative curves (Fig. S2). Thus, linker decomposition starts at 583 K in pure **M-1**, while for **HM-1** and **HM-2**, the process starts at 563 K and 553 K, respectively.

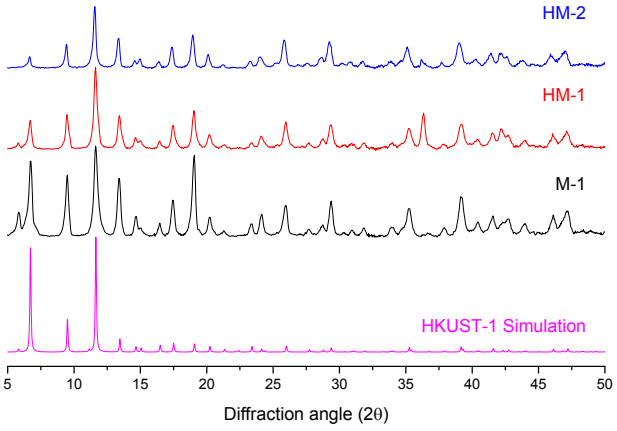

Figure 1. XRD patterns (CuKα1 radiation) of pristine HKUST-1 (**M-1**) and hierarchically structured samples **HM-1** and **HM-2**.

Following the method reported by Valenzano et. al,[30] the TGA curves were also used to estimate the relative metal-to-linker content of the materials, which allow us to determine whether ligand or metal defects (which are not mutually exclusive) predominate within a material, and in what proportion. Combining this information with the data coming from ICP (Cu) and elemental analysis (C, H, N), the chemical composition and empirical formulas of the samples were determined, and the results are summarized in Table 1 (and related information in the Supplementary Material).

Table 1. Empirical formulas and missing linker defects determined for the samples.

	Empirical Formula	Missing linkers
M-1	$[Cu_3(BTC)_{1.94}]$	3.0%
HM-1	$[Cu_3(BTC)_{1.73}(OH\text{-}IP)_{0.19}(NO_3)_{0.19}]$	4.0%
HM-2	$[Cu_3(BTC)_{1.54}(OH\text{-}IP)_{0.27}(NO_3)_{0.27}]$	9.5%

The empirical formula of "ideal", defect-free HKUST-1 is $[Cu_3BTC)_2]$. However, it is well known that "real" MOFs usually contain structural defects, such as missing linkers, missing metallic nodes, or both types of defects simultaneously. These missing units all contribute to enhance the porosity of the defective material (*vide infra*). According to our TGA analysis, the total amount of organic linkers (BTC+OH-IP) in all the samples prepared is lower than 2, the value expected from the theoretical formula for "ideal" HKUST-1, indicating that in all of them there is a neat predominance of missing linker defects over missing metallic nodes. The calculated net amount of missing linker defects is quite low in **M1** and **HM-1** (3-4%), and it increases significantly in **HM-2** (up to 9.5%).

Moreover, when mixed-linker MOFs are prepared by combining BTC^{-3} linkers with ditopic $OH\text{-}IP^{-2}$, as in **HM-1** and **HM-2** samples, the excess charge of the missing carboxylate of OH-IP with respect to trivalent BTC^{-3} linkers can be compensated by: i) residual anions (NO_3^-) coming from the copper nitrate used in the synthesis, ii) mixed-valence Cu^+/Cu^{2+} species, or iii) missing Cu_2 paddlewheel nodes. Since TGA has shown that there are less metallic nodes defects than linker defects, and FTIR spectroscopy of adsorbed CO revealed that the amounts of Cu^+ centers in all samples are similar and very low (see discussion below), it is assumed that charge defect upon OH-IP incorporation is mainly compensated by residual nitrate anions, as it has been reflected in the calculated empirical formulas shown in Table 1.

The textural properties of the samples were then evaluated from the N_2 adsorption-desorption isotherms at 77 K, and the curves obtained are shown in Fig. 2. Pristine **M-1** sample exhibits a clear type-I isotherm,[31] with a sharp increase in the N_2 uptake at low relative pressure, followed by a plateau, typical of microporous HKUST-1.[32] A small hysteresis loop, akin to H3 o H4 type according to the IUPAC classification,[33] is observed at high relative pressures, indicating the presence of interparticle porosity.

Conversely, **HM-1** and **HM-2** show distinctly different, type IV isotherms, with well-defined H2 type hysteresis loops at relative pressures of $P/P_0 > 0.4$, indicating capillary condensation of N_2 in mesopores. Thus, these results prove the coexistence of a hierarchical system of micro- and mesopores in mixed-linker **HM-1** and **HM-2** samples.

Table 2 shows a summary of the textural properties for the samples, calculated as detailed in the Experimental section.

View Article Online
DOI: 10.1039/D6MA00417B

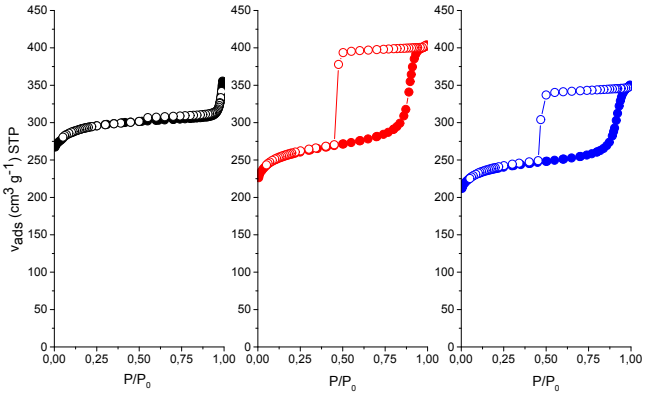

Figure 2. N_2 adsorption-desorption isotherms (at 77 K) of (from left to right): **M-1**, **HM-1** and **HM-2** samples.

Table 2. Textural properties of the samples.

	S_{BET} (m^2 g^{-1})[a]	Pore volume (cm^3 g^{-1}) V_{tot}[b]	V_{micro}[c]	V_{meso}[d]	Pore diameter (nm)
M-1	1166	0.550	0.449	0.036	No mesopores
HM-1	1008	0.625	0.371	0.240	1.98
HM-2	939	0.542	0.351	0.149	2.48

[a] S_{BET}: Brunnauer-Emmett-Teller surface area. Only data points satisfying the Rouquerol consistency criterion have been considered; [b] V_{total}: total pore volume, calculated from the nitrogen adsorption data at P/P_0=0.995; [c] V_{micro}: micropore volume obtained by the t-plot method; [d] V_{meso}: mesopore volume calculated by the Barrett-Joyner-Halenda (BJH) method.

According to the data presented in Table 2, incorporation of OH-IP linker into the crystalline framework of HKUST-1 produces a gradual decrease of the S_{BET} area with respect to pristine sample. This can be attributed to an increase of the pore size in hierarchical MOFs,[9] which in the case of **HM-1** and **HM-2** are 1.98 and 2.48 nm, respectively. S_{BET} values can also be affected by a decrease of the crystallinity of **HM-1** and **HM-2** samples due to the formation of structural defects induced by the introduction of the secondary linker in the structure.[18] Indeed, the presence of mesopores accompanied by a certain loss of specific surface area has been previously observed in many works related with the preparation of mixed-linker MOFs and other compounds.[9,18,22–26,34] While **M-1** is basically microporous (V_{meso} = 0.036 cm^3 g^{-1}), HM-1 and HM-2 samples exhibit a significant mesopore volume, accounting for up to 40% of the total pore volume in **HM-1** and slightly lower 30% in **HM-2**.

In comparison to other pristine and mixed-linker HKUST-1 samples prepared with the OH-IP ligand as reported by other researchers, [17] our synthesized materials exhibit notably lower specific surface areas and total pore volume values. For instance, 1882 m^2g^{-1} and 0.773 cm^3g^{-1}, contrasting with 1166 m^2g^{-1} and 0.550 cm^3g^{-1} for pristine HKUST-1, and SBET values of approximately 1700-1800 m^2g^{-1} and pore volumes of about 0.75 cm^3g^{-1}, compared to surface areas of around 1000 m^2g^{-1} and pore volumes of 0.54-0.62 cm^3g^{-1}. These disparities are significant and are likely attributable to reduced crystallinity and the potential incorporation of amorphous material within our samples, relative to those synthesized by Fang et al.[17] Formation of mesopores in mixed-linker HKUST-1 has been previously reported by Fang et. al.[17] Incorporation of OH-IP linkers into the crystalline framework introduced a charge excess due to the different charge of $[BTC]^{3-}$ and $[OH\text{-}IP]^{2-}$ linkers. The authors proposed that charge excess can be compensated by either the partial reduction of Cu^{2+} to Cu_+ in the inorganic building blocks, or by the presence of missing linker defects or missing copper nodes. Both mechanisms would result in the formation of local defects, which subsequently facilitate the creation of mesopores through their clustering. Nevertheless, the authors did not determine in their original work whether the introduction of OH-IP defective linkers and creation of mesopores in mixed-linkers HKUST-1 induced any alterations in particle morphology.

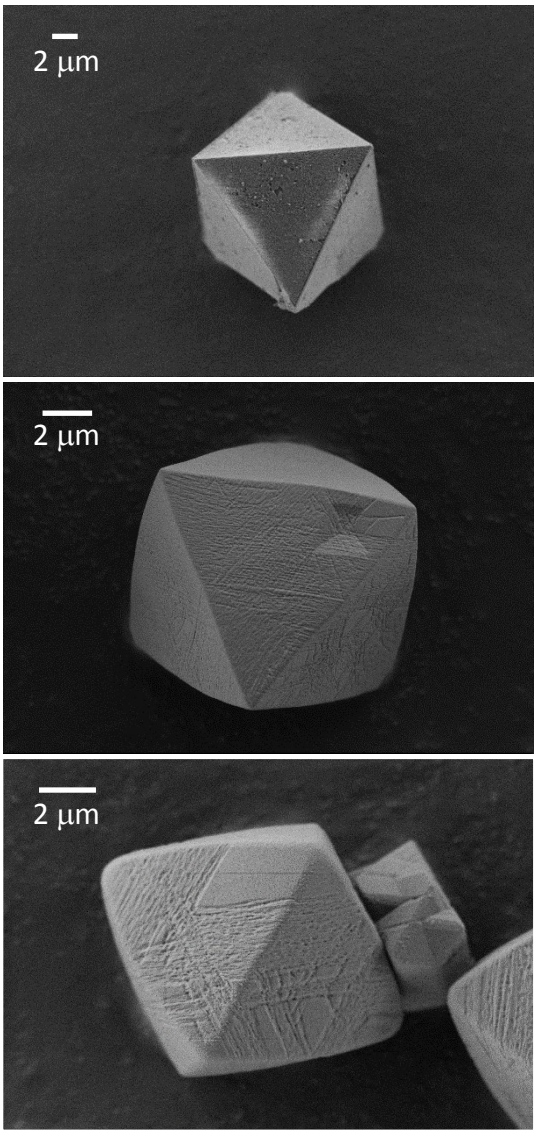

Figure 3. FESEM images of (from *top* to *bottom*): **M-1**, **HM-1** and **HM-2**.

Figs. 3 and Fig. S3 show FESEM images of **M-1**, **HM-1** and **HM-2** samples, respectively. As it can be seen, **M-1** exhibits well formed octahedral crystallites typical of HKUST-1 materials, with sharp edges and some inherent defects on their faces, formed during the crystallization process.[35] The same morphology is also observed for mixed-linker **HM-1** and **HM-2** samples, though surface defects become gradually more evident and ordered upon OH-IP incorporation, while the edges of the octahedra become more rounded.

Other authors have also reported important morphology changes in HKUST-1 prepared in the presence of benzoic acid or citric acid modulators.[18,36] In those cases, the authors described the formation of relatively big holes randomly distributed on the surface of the octahedral crystals. Interestingly, the type of defects created in **HM-1** and **HM-2** upon incorporation of OH-IP linkers are clearly not-randomly distributed on the crystallite faces, in evident contrast with the meso/macropores created during the synthesis with benzoic or citric acid modulators. Instead, these defects tend to coalesce into extensive linear trenches that run parallel to the edges of the octahedral crystals. The observed trenches in **HM-1** and **HM-2** exhibit a resemblance to defect lines also oriented parallel to the octahedral edges, as reported by Shöâeè et al.,[35,37] and by Ameloot et al.,[38] using atomic force microscopy (AFM) and *operando* confocal fluorescence microscopy, respectively. The authors attributed the formation of these defect lines to dislocations of the crystalline network along the <110> direction. Projection of the HKUST-1 structure along the <110> direction evidences two potential surface terminations for the {111} planes (corresponding to triangular faces of the octahedra) that do not involve the cleavage of intramolecular bonds within the BTC linkers. Of these two viable surface terminations, the one depicted in Fig. 4 is considered the most feasible, wherein only a single carboxylate group per BTC linker remains unbound to the bulk crystal structure.

It is logical to postulate that OH-IP linkers, possessing only two carboxylate groups as opposed to the three found in BTC, may preferentially occupy these sites at the {111} surface terminations. Consequently, the hydroxyl group of OH-IP (represented by a large green sphere in the figure) would extend outwards from the triangular faces of the octahedral crystals, while the linker would maintain its connection to the crystal via the two remaining carboxylate groups. Therefore, as the amount of OH-IP incorporated within the solid network increases (passing from **HM-1** to **HM-2**), a higher concentration of defective linkers at these surface termination sites is anticipated. This observation may account for the formation of extended line defects that run parallel to the edges of the octahedral crystals, In other words, the analysis of the surface morphology of our mixed-linker samples have revealed that the distribution of OH-IP linkers within the HKUST-1 crystal lattice would not be random but rather ordered along defect lines, thereby leading to the formation of broad and deep trenches evidenced in the aforementioned FESEM images.

We have carefully evaluated relative peak intensities and peak width of all the diffraction lines in all three samples, but we have not found any clear correlation with the amount of OH-IP linker incorporation. This might be related to the relatively low substitution of OH-IP linkers in samples HM-1 and HM-2, but not only. Note that incorporation of OH-IP linker in the HKUST-1 lattice can disrupt the crystal growth of the MOF in the direction where the OH groups are oriented, giving rise to the formation of the wide trenches observed in the FESEM images, but without affecting the crystallographic planes underneath these terminations. A much more detailed diffraction analysis, probably combined with other advanced techniques more sensitive to surface atoms (such as SEXAFS) and quantum chemical calculations, would be required to determine this point, which falls beyond the scope of the present paper.

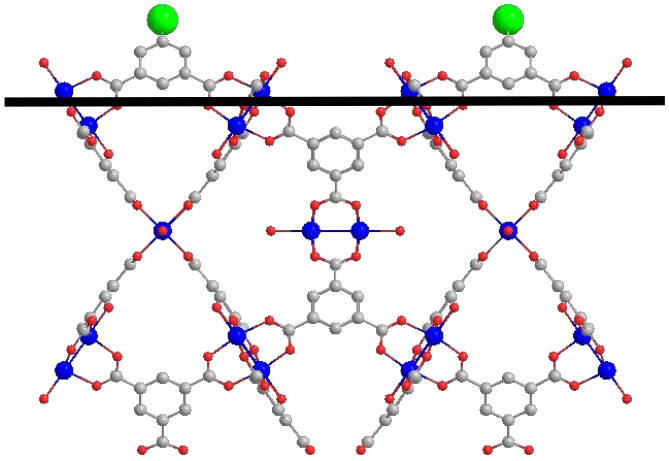

Figure 4. Structure of HKUST-1 viewed along the <110> direction, showing the most likely surface termination at the {111} faces. The green spheres represent the dangling hydroxy groups of OH-IP linkers pointing outwards from the triangular faces of the octahedral crystals, while the broad black line represents the terminations of these triangular {111} faces.

3.2. Synthesis of quinazoline

As mentioned before, we selected the formation of a bulky compound as a test reaction to evaluate the benefits of a hierarchical micro-/mesopore system in mixed-linker HKUST-1. Thus, herein we have carried out the oxidative synthesis of quinazoline from 2-aminoacetophenone and benzylamine in the presence of **M-1**, **HM-1** and **HM-2** catalysts, using TBHP as the oxidant in DMSO at 353 K (Scheme 1). The results obtained up to 5 h of reaction time are shown in Fig. 5. A blank experiment (without using any catalyst) was also performed under the same reaction conditions, but no quinazoline yield was obtained even after extending the reaction for 8 h.

View Article Online
DOI: 10.1039/D6MA00447B

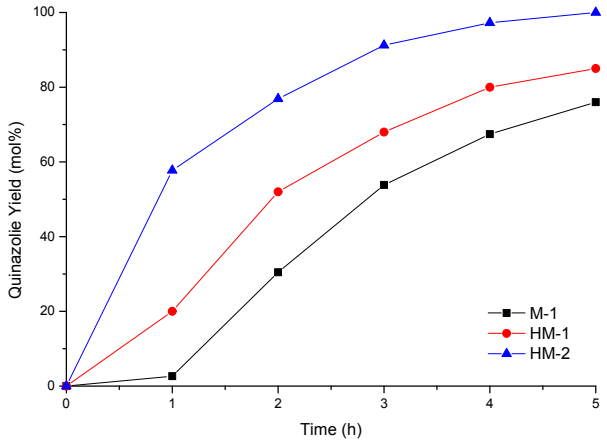

Figure 5. Time-yield plot of oxidative quinazoline synthesis over **M-1**, **HM-1** and **HM-2** catalysts.

All three compounds showed good activity and quantitative selectivity to quinazoline, and no other products were detected. However, a definite increase of the reaction rate and final conversion was observed upon increasing the amount of OH-IP incorporated into the MOF structure. Thus, the yield obtained after 3 h of reaction was 54%, 68% and 91% for **M-1**, **HM-1** and **HM-2** catalysts, respectively. While **M-1** showed a clear induction period of approximately 1 h prior to quinazoline formation, this lag phase was progressively suppressed for the hierarchically structured MOFs. The sample **HM-2**, containing 15% of OH-IP incorporated in the framework, demonstrated the best catalytic performance, achieving a quinazoline yield of 100% within 5 hours. Therefore, this catalyst was selected for further evaluation.

The scope of the reaction was evaluated by applying the process to the synthesis of other quinazolines, including bulkier substrates, such as 2-aminobenzophenone, as well as substituted benzylamines with electron donating or electron withdrawing groups in *para* position (Table S1). In all cases, the reaction was 100% selective to the corresponding quinazoline derivatives, while the presence of mesoporosity in **HM-2** ensured excellent yields for all the compounds tested.

To demonstrate the heterogeneous character of the reaction and to exclude the possibility of active species leaching from the solid phase into the liquid reaction medium, a hot filtration experiment was carried out during the course of the reaction. Thus, the quinazoline synthesis reaction was carried out under the same reaction conditions for 0.5 h in the presence of **HM-2**. At this point, with a 24% quinazoline yield, the solid catalyst was separated from the reaction mixture by filtration at the reaction temperature, and reaction was continued for an additional 4.5 h in the absence of the catalyst. The results obtained (Figure S4) showed that the reaction almost completely stopped after the catalyst was removed, with practically no further quinazoline formation observed. Furthermore, the ICP analysis of the filtrate after the reaction indicates that no significant leaching of the active copper species took place. These results clearly show that the cyclization reaction between 2-aminoacetophenone and benzylamine only proceeds in the presence of the catalyst and that the process is truly heterogeneous.

Finally, we evaluated the reusability of the catalyst. Thus**, HM-2** was reused in consecutive catalytic cycles under identical reaction conditions. After each run for 5 h, the solid was recovered by centrifugation, washed with fresh DMSO and acetone, dried overnight at room temperature under a vacuum and reused in consecutive cycles.

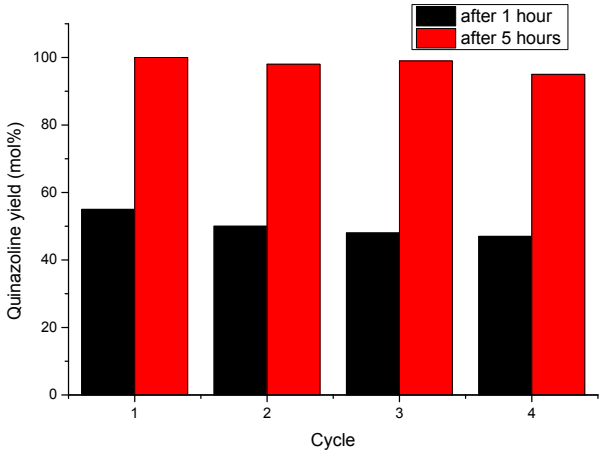

Figure 6. Reusability of **HM-2** after 1 h and 5 h of reaction time.

As shown in Fig. 6, **HM-2** showed an excellent reusability for at least four cycles, with only a minor loss of activity and keeping the full selectivity to quinazoline. Thus, quinazoline yield after 1 h gradually decreases from 55% in the first cycle to 47% in the fourth cycle, while the full conversion after 5 h is maintained in all runs. The XRD pattern of the solid recovered after four catalytic runs (Fig. S5) showed a small decrease of the intensity of the diffraction peaks with respect to the fresh material, which is probably due to the adsorption of reaction products on the surface of the catalysts that are not completely removed during the washing procedure, though some actual crystallinity loss can also take place due to the mechanical attrition of the particles during the reaction. Nevertheless, the overall structure integrity of the catalyst is clearly preserved throughout all the uses.

Based on previous related studies, a plausible mechanism to explain the one-pot formation of quinazoline through oxidative coupling of benylamine and 2-aminoacetophenone is depicted in Scheme 2.

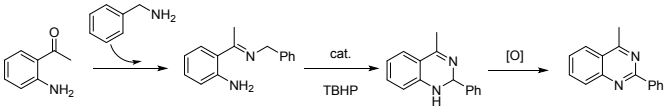

Scheme 2. Mechanism of the oxidative coupling synthesis of quinazoline.

View Article Online
DOI: 10.1039/D6MA00417B

First, an intermediate imine product is formed by condensation of 2-aminoacetophenone and benzylamine. This step is almost immediate and it can take place under catalyst free conditions. However, the coordinatively unsaturated Cu^{2+} sites in HKUST-1 can act as Lewis acid sites to accelerate even further this step. Then, the imine intermediate undergoes oxidized cyclization reaction in the presence of TBHP, which finally yields the target quinazoline product by oxidative dehydrogenation.

3.3. Origin of the higher catalytic activity of hierarchically structured MOFs

Several authors have reported on the use of defective linkers to improve the catalytic performance of MOFs as well as a means of introducing new properties which are totally absent in the unmodified, pristine material.[4,19,39] In most cases, the improvement of the catalytic properties of mixed-linker MOFs is attributed to the creation of point defects, leading to the creation of more exposed and/or more reactive active sites. In the particular case of compounds with the HKUST-1 structure, creation of mixed-valence copper or ruthenium centers upon incorporation of defective linkers were deemed responsible for the higher reactivity in the oxidation of benzene derivatives,[40] olefin hydrogenation, CO_2 reduction [12] or Paal-Knorr synthesis of pyrrole.[13] Thus, a similar effect might also be behind the higher catalytic activity of mixed-linker compounds for the synthesis of quinazoline observed in the present work. In other words, partial substitution of BTC by OH-IP linkers can create defective sites similar to these observed in other mixed-linker MOFs. However, FTIR spectroscopy of adsorbed CO at 77 K onto **M-1** and HM-2 (see Fig S6) revealed that no significant differences exist in the type, amount or accessibility of the active sites in both materials. Thus, we did not observe any higher amount of reduced Cu^{+} sites in **HM-2** than in **M-1** as a consequence of the introduction of OH-IP linkers in the framework, since this would be seen in appreciable changes in relative intensities of the corresponding IR absorption bands upon CO adsorption on these reduced sites. Thus, even if the creation of a small population of partially reduced sites cannot be totally excluded, the higher activity of **HM-2** for the quinazoline synthesis may have a different origin.

In our opinion, the catalytic results shown in Fig. 5 and Table S1 can be explained by the presence in **HM-1** and **HM-2** of a hierarchical micro-/mesopore system. While the reagents benzylamine and 2-aminoacetophenone used in this reaction are small enough to enter and freely diffuse inside the pores of HKUST-1 (with diameter of ca. 9 Å), this is not so for the bulky quinazoline product, with approximate dimensions 12 x 8 x 3 $Å^3$, very close to the pore openings of the MOF. Thus, once quinazoline is formed inside the MOF pores (where the active sites are located), strong diffusion limitations are anticipated for its desorption,[5] increasing the time of residence of the reaction products inside the pores and partially blocking the access of fresh reactants to the active sites. However, the presence of a mesopore system in mixed-linker **HM-1** and **HM-2** (accounting for up to 40% of the total pore volume of the material) can provide alternative diffusion pathway for a fast quinazoline desorption, thus minimizing the unwanted pore-blocking, which would translate into a higher reaction rate, as it is schematically depicted in Fig. 7.

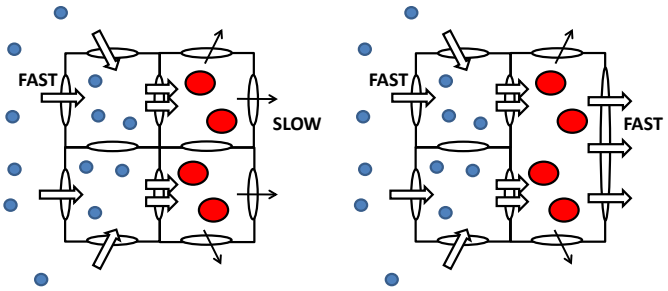

Figure 7. Diffusion of small reactants (blue spheres) and bulky products (red spheres) in pristine microrporous **M-1** (*left*) and hierarchical mesoporous-mesoporous materials **HM-1** and **HM-2** (*right*).

Besides the afore mentioned benefits of the creation of a hierarchical mesopore system in mixd-linker MOFs, other factors might contribute as well to the observed catalytic properties of **M-1** vs **HM-1/HM-2**. One of them could be particle size: smaller crystallites would reduce the diffusion path length, thereby minimizing mass transport limitations. However according to the FESEM images shown in Fig. 3 (and additional images shown in Fig. S3), the average particle size if close to 10-12 μm for all compounds. With no significant differences among them. Moreover, the relatively large particle size of all three materials indicates that most active sites are located in the internal surface of the catalysts, so that the contribution from external sites to the overall catalytic activity is expected to be low.

Conclusion

Herein we describe the preparation of isoreticular mixed-linker HKUST-1 materials in which the parent BTC linker has been partially replaced by a defective-inducing ditopic linker, OH-IP. As a result, a hierarchical micro-/mesoporous system is formed, in which mesopores accounts for up to 40% of the total pore volume, accompanied by a slight decrease of the specific surface area (S_{BET}), from 1166 to 939 $m^2 g^{-1}$. A close inspection of the morphology of the crystals by means of FESEM showed that mesopores are well visible in the form of deep trenches that run parallel to the edges of the octahedral crystals. These trenches are compatible with dislocations along the <1 1 0> direction, which would lead to preferential surface terminations in the {1 1 1} faces in which the linker are bound to the bulk crystals by only two carboxylate groups, while the third one is dangling. It is reasonable that these terminal positions be preferentially occupied by ditopic OH-IP linkers, since as the amount of OH-IP incorporated into the framework increases, the number and depth of the trenches is also seen to increase.

Pristine and mixed-linker HKUST-1 have been tested for the catalytic oxidative coupling of benzylamine and 2-aminoacetophenone to form quinazoline, using TBHP as the oxidant. A progressive increase of the reaction rate is observed paralleling the amount of OH-IP substitution, which we attribute to the presence of a mesopore

system that mitigate diffusion limitations for the desorption of the bulky quinazoline product formed inside the MOF pores.

Author contributions

A.N.: Investigation, Writing – original draft; FXLX: Conceptualization, Funding acquisition, Writing – review & editing.

Conflicts of interest

There are no conflicts to declare.

Data availability

The data supporting this article have been included as part of the Supplementary Information. Supplementary information: Tables S1 (scope of the reaction), Figures S1-S6 (^{1}H NMR spectra of acid digested **HM-1** and **HM-2**; TGA curves; representative FESEM images of all samples; hot-filtration test; XRD pattern of fresh and used **HM-2**; and FTIR spectra of adsorbed CO onto **M-1** and **HM-2**). All data will also made available at the institutional repositories of the authors: Riunet (https://riunet.upv.es/home) and digital CSIC (https://digital.csic.es/).

Acknowledgements

Financial support from the Spanish Ministry of Science and Innovation (PID2023-146114NB-C21, and CEX2021-001230-S grants funded by MCIN/AEI/10.13039/501100011033) is gratefully acknowledged. This study forms part of the Advanced Materials Program and was supported by MICIN with funding from European Union NextGeneration (PRTR-C17.I1) and by the Generalitat Valenciana (MFA/2022/003).

1 A. Corma, H. Garcia and F. X. Llabrés i Xamena, *Chem. Rev.*, 2010, **110**, 4606–4655.

2 J. Gascon, A. Corma, F. Kapteijn and F. X. Llabrés i Xamena, *ACS Catal.*, 2014, **4**, 361–378.

3 S. M. J. Rogge, A. Bavykina, J. Hajek, H. Garcia, A. I. Olivos-Suarez, A. Sepúlveda-Escribano, A. Vimont, G. Clet, P. Bazin, F. Kapteijn, M. Daturi, E. V Ramos Fernandez, F. X. Llabrés i Xamena, V. Van Speybroeck and J. Gascon, *Chem. Soc. Rev.*, 2017, **46**, 3134–3184.

4 H.-H. Mautschke, F. Drache, I. Senkovska, S. Kaskel and F. X. Llabrés i Xamena, *Catal. Sci. Technol.*, 2018, **8**, 3610–3616.

5 B. R. Saifutdinov, V. I. Isaeva, V. V. Chernyshev, V. V. Vergun, G. I. Kapustin, Y. P. Ivanova, M. M. Ilyin, O. P. Tkachenko, A. K. Buryak and L. M. Kustov, *Polymers (Basel).*, 2022, **14**, 1373.

6 Y. Q. Lan, H. L. Jiang, S. L. Li and Q. Xu, *Advanced Materials*, 2011, **23**, 5015–5020.

7 H. L. Jiang, Y. Tatsu, Z. H. Lu and Q. Xu, *J. Am. Chem. Soc.*, 2010, **132**, 5586–5587.

8 H. Y. Guan, R. J. LeBlanc, S. Y. Xie and Y. Yue, *Coord. Chem. Rev.*, 2018, **369**, 76–90.

9 J. Park, Z. U. Wang, L. B. Sun, Y. P. Chen and H. C. Zhou, *J. Am. Chem. Soc.*, 2012, **134**, 20110–20116.

10 Z. Fan, J. Wang, W. Wang, S. Burger, Z. Wang, Y. Wang, C. Wöll, M. Cokoja and R. A. Fischer, *ACS Appl. Mater. Interfaces*, 2020, **12**, 37993–38002.

11 W. R. Heinz, R. Junk, I. Agirrezabal-Telleria, B. Bueken, H. Bunzen, T. Gölz, M. Cokoja, D. De Vos and R. A. Fischer, *Catal. Sci. Technol.*, 2020, **10**, 8077–8085.

12 O. Kozachuk, I. Luz, F. X. Llabrés i Xamena, H. Noei, M. Kauer, H. B. Albada, E. D. Bloch, B. Marler, Y. Wang, M. Muhler and R. A. Fischer, *Angew. Chem. Int. Ed.*, 2014, **53**, 7058–7062.

13 W. Zhang, M. Kauer, O. Halbherr, K. Epp, P. Guo, M. I. Gonzalez, D. J. Xiao, C. Wiktor, F. X. Llabrés i Xamena, C. Wöll, Y. Wang, M. Muhler and R. A. Fischer, *Chemistry-a European Journal*, 2016, **22**, 14297–14307.

14 S. He, Y. Chen, Z. Zhang, B. Ni, W. He and X. Wang, *Chem. Sci.*, 2016, **7**, 7101–7105.

15 K. M. Choi, H. J. Jeon, J. K. Kang and O. M. Yaghi, *J. Am. Chem. Soc.*, 2011, **133**, 11920–11923.

16 Z. Xin, J. Bai, Y. Pan, M. J. Zaworotko, Z. Xin, J. Bai, Y. Pan and M. J. Zaworotko, *Chemistry – A European Journal*, 2010, **16**, 13049–13052.

View Article Online
DOI: 10.1039/D6MA00417B

17 Z. Fang, J. P. Dürholt, M. Kauer, W. Zhang, C. Lochenie, B. Jee, B. Albada, N. Metzler-Nolte, A. Pöppl, B. Weber, M. Muhler, Y. Wang, R. Schmid and R. A. Fischer, *J. Am. Chem. Soc.*, 2014, **136**, 9627–9636.

18 B. Liu, Y. Li, S. C. Oh, Y. Fang and H. Xi, *RSC Adv.*, 2016, **6**, 61006–61012.

19 H. H. Mautschke and F. X. Llabrés i Xamena, *Chemistry – A European Journal*, 2021, **27**, 10766–10775.

20 G. A. Khodarahmi, E. Jafari, M. R. Khajouei, F. Hassanzadeh, G. H. Hakimelahi and G. A. Khodarahmi, *Res. Pharm. Sci.*, 2016, **11**, 1–14.

21 P. Kushwaha, A. Bhardwaj and Rashi, *Tetrahedron*, 2025, **179**, 134635.

22 C. Wang, S. Li, H. Liu, Y. Jiang and H. Fu, *Journal of Organic Chemistry*, 2010, **75**, 7936–7938.

23 B. Han, X. L. Yang, C. Wang, Y. W. Bai, T. C. Pan, X. Chen and W. Yu, *Journal of Organic Chemistry*, 2012, **77**, 1136–1142.

24 N. Anand, K. H. P. Reddy, T. Satyanarayana, K. S. R. Rao and D. R. Burri, *Catal. Sci. Technol.*, 2012, **2**, 570–574.

25 H. Yuan, W. J. Yoo, H. Miyamura and S. Kobayashi, *Adv. Synth. Catal.*, 2012, **354**, 2899–2904.

26 T. Truong, T. M. Hoang, C. K. Nguyen, Q. T. N. Huynh and N. T. S. Phan, *RSC Adv.*, 2015, **5**, 24769–24776.

27 J. Rouquerol, P. Llewellyn and F. Rouquerol, *Stud. Surf. Sci. Catal.*, 2007, **160**, 49–56.

28 D. A. Gómez-Gualdrón, P. Z. Moghadam, J. T. Hupp, O. K. Farha and R. Q. Snurr, *J. Am. Chem. Soc.*, 2016, **138**, 215–224.

29 E. P. Barrett, L. G. Joyner and P. P. Halenda, *J. Am. Chem. Soc.*, 1951, **73**, 373–380.

30 L. Valenzano, B. Civalleri, S. Chavan, S. Bordiga, M. H. Nilsen, S. Jakobsen, K. P. Lillerud and C. Lamberti, *Chemistry of Materials*, 2011, **23**, 1700–1718.

31 K. S. W. Sing, D. H. Everett, R. A. W. Haul, L. Moscou, R. A. Pierotti, J. Rouquerol and T. Siemieniewska, *Pure and Applied Chemistry*, 1985, **57**, 603–619.

32 S. S. Y. Chui, S. M. F. Lo, J. P. H. Charmant, A. G. Orpen and I. D. Williams, *Science (1979).*, 1999, **283**, 1148–1150.

33 M. Thommes, K. Kaneko, A. V. Neimark, J. P. Olivier, F. Rodriguez-Reinoso, J. Rouquerol and K. S. W. Sing, *Pure and Applied Chemistry*, 2015, **87**, 1051–1069.

34 X. Yang, L. Qiao and W. Dai, *Chinese Journal of Catalysis*, 2015, **36**, 1875–1885.

35 M. Shoaee, M. W. Anderson and M. P. Attfield, *Angew. Chem. Int. Ed.*, 2008, **47**, 8525–8528.

36 T. Liu, Y. Liu, L. Yao, W. Yang, L. Tian, H. Liu, D. Liu and C. Wang, *Nanoscale*, 2018, **10**, 13194–13201.

37 M. Shöâeè, J. R. Agger, M. W. Anderson and M. P. Attfield, *CrystEngComm*, 2008, **10**, 646–648.

38 R. Ameloot, F. Vermoortele, J. Hofkens, F. C. De Schryver, D. E. De Vos and M. B. J. Roeffaers, *Angew. Chem. Int. Ed.*, 2013, **52**, 401–405.

39 H. H. Mautschke and F. X. Llabrés i Xamena, *Molecules*, 2022, **27**, 6315.

40 S. Marx, W. Kleist and A. Baiker, *J. Catal.*, 2011, **281**, 76–87.

View Article Online
DOI: 10.1039/D6MA00417B

Data availability

The data supporting this article have been included as part of the Supplementary Information. Supplementary information: Tables S1 (scope of the reaction), Figures S1-S6 (^{1}H NMR spectra of acid digested **HM-1** and **HM-2**; TGA curves; representative FESEM images of all samples; hot-filtration test; XRD pattern of fresh and used **HM-2**; and FTIR spectra of adsorbed CO onto **M-1** and **HM-2**). All data will also made available at the institutional repositories of the authors: Riunet (https://riunet.upv.es/home) and digital CSIC (https://digital.csic.es/).